Optical Fiber Technology 75 (2023) 103192

Contents lists available at ScienceDirect

Optical Fiber Technology

journal homepage: www.elsevier.com/locate/yofte

Detailed spatial-spectral numerical characterization of axially symmetric broadband ultrasonic resonances in standard optical fibers

Ricardo E. da Silva *, David J. Webb

Aston Institute of Photonic Technologies, Aston University, Birmingham B4 7ET, UK

ARTICLE INFO

Keywords:
Fiber-optic acoustic devices
Optoacoustic fiber sensors
Acousto-optic modulators
High frequency ultrasound
Numerical analysis
Finite element method

ABSTRACT

Standard single mode optical fibers (SMFs) have been widely employed to generate and measure ultrasonic signals in remarkable applications. In particular, optoacoustic fiber sensors provide unique features for micro-scale high resolution ultrasound imaging in biomedicine. However, at specific resonance frequencies, SMFs work as acoustic filters inducing relevant geometrical attenuation bands higher than 10 dB, which limit the sensors' sensitivity and frequency operation, causing image distortions and artifacts. We have numerically demonstrated high frequency axially symmetric ultrasonic resonances inside an optical fiber for the first time. The propagation of resonant axially symmetric acoustic modes along 1 cm fiber is investigated by means of 2D and 3D finite element techniques up to 80 MHz. The dispersion of the modes and induced beatlengths are characterized from the complex multimode interference with the 2D Fourier transform. The simulated spectra are validated with the renowned Pochhammer-Chree analytical equations. The frequency response of the acoustically induced strains in the fiber core is evaluated, and important acoustic parameters relevant for the modulation of phase, wavelength and power in optical fibers and diffractive gratings are derived and discussed. The results show that these resonances are strongly dependent on the modal beatlengths. Solutions to improve the operation of fiber-based devices are proposed, pointing out new alternatives to advance broadband optoacoustic sensors and monolithic acousto-optic modulators.

1. Introduction

Acoustic waves have been successfully employed to modulate the phase, wavelength, and power in optical fibers, which is attractive for the development of all-fiber acousto-optic modulators and fiber-optic acoustic sensors. For optical modulation, a piezoelectric driver usually generates the acoustic waves that are amplified by an acoustic horn to propagate along a fiber segment. The acousto-optic interaction enables electrically-tunable notch filters, frequency shifters, couplers, mode-locked and Q-switched pulsed fiber lasers [1–8]. Similarly, the acoustic signals from a variety of ultrasonic sources, such as, partial discharges in high-voltage electric machines, aircrafts, rail trains, mechanical engines, civil infrastructure, and even vital human organs and tissues, are efficiently characterized employing fiber sensors [9–18]. However, distortion and resonance of acoustic signals in the fibers with increasing frequency have limited the advance of current fiber-based devices, demanding increasing computer-based techniques to evaluate complex acoustic fields and modulated optical properties.

Fiber acoustic resonances have been widely investigated at frequencies from kilohertz [19] up to hundreds of megahertz, such as, resonances generated by optically induced non-linear effects [20,21]. In general, these resonances originate from distinct physical mechanisms and acoustic modes and have usually a narrow bandwidth. In contrast, the interference of axially symmetric modes induces wide spectral bands from 10 MHz. Such resonances and frequency range have been partially analytically and experimentally investigated, but not numerically [15–18]. These previous studies do not model or evaluate the acoustic modes, their interaction and contribution to form the resonant bands. Although axially symmetric modes have been individually evaluated in a multimode fiber, that study does not consider modal interference and beatlengths and, consequently, the resonances cannot be determined [22]. The propagation of acoustic modes in optical fibers has been analytically evaluated to facilitate the development of acousto-optic modulators, and in the low dispersive frequency range up to 10 MHz, the fundamental acoustic mode, which induces constant sinusoidal waveforms, has been fully characterized [22]. The advance of fiber-optic technology and development of micro-components have contributed to the fabrication of modulators operating at frequencies up to 10.9 MHz

* Corresponding author.
E-mail address: r.da-silva@aston.ac.uk (R.E. da Silva).

https://doi.org/10.1016/j.yofte.2022.103192
Received 19 September 2022; Received in revised form 8 November 2022; Accepted 30 November 2022
Available online 12 December 2022

[23]. The interaction of axially symmetric acoustic modes and fiber Bragg gratings (FBGs) allows the dynamic modulation of the grating reflection properties, mode-locking the output power of pulsed fiber lasers [6,7]. The laser repetition rate is electrically tunable at twice the acoustic frequency. Nevertheless, the current acousto-optic devices are essentially limited by decreasing concentration of acoustic energy in the fiber core with increasing frequency beyond 10 MHz.

The high sensitivity of FBGs to strain and temperature has also expanded the development of passive fiber-optic devices, such as opto-acoustic sensors for biomedical applications, where ultrasonic waves are generated by thermoelastic expansion of biological tissues [15–18]. The acoustically induced strains change the refractive index in the fiber core inducing phase-shifts in the guided light. High resolution optoacoustic sensors based on π-phase-shifted Bragg gratings (π-FBGs) have been reported, offering acoustic sensitivities up to 18 times higher compared to the traditional piezoelectric devices. The π-phase-shifted optical cavities ranging from 270 to 350 μm in length significantly reduce the grating's effective sensing areas, increasing the sensor's spatial resolution [17,18]. However, the sensor's response is dominated by radial and circumferential resonances inducing sensitivity peaks around 20 - 25 MHz, followed by the high attenuation range of 40 - 60 MHz [15,17,24]. This attenuation band and other emergent resonant peaks around 30 and 70 MHz observed in the practical devices are not fully explained and characterized.

Analytical and semi-analytical methods based on the scattering of elastic waves have been employed to simulate the frequency response of optoacoustic devices. The methods however consider only the integration of the acoustic fields in the fiber core center [15,17]. In general, modeling of acoustic wave propagation in optical fibers is highly elaborate and strictly developed for ideal, homogeneous, and solid cylinders [25,26]. The methods cannot usually be applied to evaluate 2D or 3D ultrasonic fields inside the fiber cross section, especially with the unusual geometries of specialty fibers [27]. Recent studies employing the finite element method (FEM) reveal that the ultrasonic fields are composed of multiple modes overlapping along the fiber [1]. The FEM is effective to model and simulate acoustic and optical components, allowing the study of entire acousto-optic devices [11,19,27–33]. The simulated acoustically induced strains in the fiber core are used in combination with the transfer matrix method to model the spectral response of devices employing FBGs [19,31]. In addition, fiber sensing substances surrounding the fiber are directly modelled by adding the component geometries, materials and physical domains [4,19,34].

In this paper, we have investigated the acoustic resonances caused by the interaction of acoustic modes propagating in an optical fiber up to 80 MHz. A novel numerical study is developed to evaluate complex ultrasonic fields in optical fibers employing the finite element method. The study is demonstrated by means of a numerical experiment and validated with the Pochhammer-Chree analytical solutions briefly presented in Section 2. A guideline for the design, modeling, and computing of 2D and 3D fiber geometries is described in Section 3. The vibration patterns of the acoustic modes are evaluated by the 2D modal analysis of the fiber cross section in Section 4. A 2D reduced-domain method is also demonstrated. The modal acoustic parameters are derived from the simulations, providing the dispersion curves for the considered frequency range. The multimode interference is evaluated from the frequency response of the 3D simulated ultrasonic fields with the 2D fast Fourier transform (FFT) in Section 5. The dispersion of the acoustic modes and induced beatlengths are evaluated in the FFT spectrum. The derived acoustic parameters are used to characterize the modal distribution and resonances inside the fiber in Section 6. The main results are discussed in Section 7, pointing to new possibilities to advance the design and fabrication of high-frequency fiber-optic ultrasonic devices.

2. Analytical modeling

2.1. Propagation and interaction of acoustic modes in standard optical fibers

The propagation of acoustic modes in solid, isotropic, homogeneous, and linearly elastic cylinders is governed by the Pochhammer-Chree theory, defining the modal dispersion by changes of the mode's wavenumber, wavelength, phase or group velocity, with the waveguide material, geometry and frequency [35,36]. The studies show that dispersion causes distortion of acoustic waves with wavelengths comparable or shorter than the cylinder diameter [37,38]. The interaction of modes propagating with different velocities along a dispersive medium attenuates and broadens the shape of acoustic signals [25,39,40].

Fig. 1(a)-(c) illustrate the vectorial composition of axially symmetric acoustic waves propagating in a standard single mode optical fiber (SMF) at frequencies of $f = 10$ MHz, $f = 30$ MHz, and $f = 50$ MHz. The acoustically induced displacement vector $\mathbf{u}$ is decomposed into radial v and axial w components. The displacements change with the SMF radial distance r from the fiber core center ($r = 0$) to the fiber surface (corresponding to the fiber radius of $r = 62.5$ μm), as illustrated in Fig. 1(d). The vector $\mathbf{u}$ is described by the equation of motion as [41],

$$\mu\nabla^2\mathbf{u} + (\gamma+\mu)\nabla\nabla\cdot\mathbf{u} = \rho\ddot{\mathbf{u}}, \tag{1}$$

where, γ and μ, are the Lame elastic constants and ρ is the mass density. $\mathbf{u}$ is decomposed into the scalar φ and vector $\boldsymbol{\psi}$ potentials as,

$$\mathbf{u} = \nabla\varphi + \nabla^{\wedge}\boldsymbol{\psi}, \tag{2}$$

where, $\nabla^2\varphi = \ddot{\varphi}c_D^{-2}$, and $\nabla^2\boldsymbol{\psi} = \ddot{\boldsymbol{\psi}}c_T^{-2}$, are respectively functions of the dilatational c_D and transversal c_T acoustic velocities, written as [42],

$$c_D^2 = \frac{\gamma+2\mu}{\rho}, \tag{3}$$

$$c_T^2 = \frac{\mu}{\rho}. \tag{4}$$

The displacements u, v and w are combined with the scalar potential φ and the three components of the vector potential $\boldsymbol{\psi}$ in Eq. (2). The radial and axial components are derived from φ and $\boldsymbol{\psi}$, as, [41],

$$v = \{-pAJ_1(pr) - \mathrm{i}kCJ_1(qr)\}\exp[\mathrm{i}(kz-\omega t)], \tag{5}$$

$$w = \{\mathrm{i}kAJ_0(pr) + qCJ_0(qr)\}\exp[\mathrm{i}(kz-\omega t)], \tag{6}$$

in which, $p^2 = \omega^2c_D^{-2} - k^2$, $q^2 = \omega^2c_T^{-2} - k^2$, $\omega = 2\pi f = kc_P$ is the angular frequency, c_P is the phase velocity, $k = 2\pi\lambda_a^{-1}$ is the wavenumber, λ_a, is the wavelength and, A and C are arbitrary constants. J_0 and J_1 are the zero and first order Bessel functions of the first kind. Achenbach, Zemanek and Redwood [38,41,43] show that replacing Eqs. (5) and (6) in stress equations, and application of traction-free boundary conditions at the guide surface, results in the Pochhammer-Chree frequency equation [41],

$$\frac{2p}{a}\left(q^2+k^2\right)J_1(pa)J_1(qa) - \left(q^2-k^2\right)^2J_0(pa)J_1(qa) - 4k^2pqJ_1(pa)J_0(qa) = 0, \tag{7}$$

also written in function of the fiber radius a and angular frequency $\omega = 2\pi f$ as [39,43,44],

$$k^2\frac{qJ_0(qa)}{J_1(qa)} - \frac{1}{2a}\left(\frac{\omega}{c_T}\right)^2 + \left[\frac{1}{2}\left(\frac{\omega}{c_T}\right)^2 - k^2\right]^2\frac{J_0(pa)}{pJ_1(pa)} = 0, \tag{8}$$

The dispersion of the acoustic modes propagating in a SMF is given by the variation of the wavenumber k with the frequency f, computed for

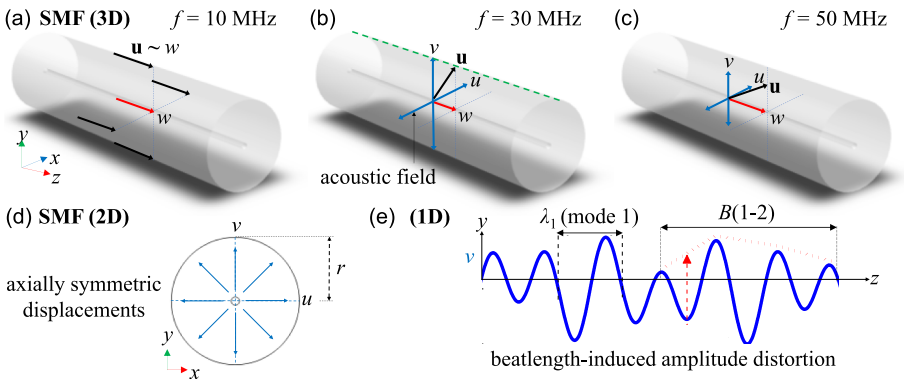

Fig. 1. Illustration of the acoustically induced displacement vector **u** decomposed into axial w and radial components, v and u, in a standard single mode optical fiber (SMF): (a) most of the displacements are axially polarized along the fiber length at $f = 10$ MHz. (b) Increased polarization of radial displacements for acoustic modes propagating with low acoustic velocities at $f = 30$ MHz. (c) Increasing axial components in the fiber for modes approaching the extensional material velocity at $f = 50$ MHz. (d) Symmetric distribution of radial components over the fiber cross section. (e) Illustration of a distorted acoustic signal evaluated at the fiber surface indicating the beatlength between two arbitrary modes along the dashed green line in Fig. 1(b). (For interpretation of the references to color in this figure legend, the reader is referred to the web version of this article.)

each acoustic mode by solving the roots of Eq. (8) (k is a real number for the propagating modes). The dispersion is also assessed considering the dimensionless wavenumber ka [41]. The phase velocity c_P of a mode approaches the material extensional velocity c_E as ka tends to zero, written as [42],

$$c_E^2 = \frac{Y}{\rho}, \tag{9}$$

where, ρ is the material density and Y is the Young's modulus. As ka tends to infinity, the modal phase velocity c_P approaches the Rayleigh surface velocity c_R, as [42],

$$c_R \sim \left(\frac{0.87 + 1.12\upsilon}{1+\upsilon}\right) c_T, \tag{10}$$

where, υ is the Poisson's ratio. The acoustic energy propagates along the fiber with the group velocity as,

$$c_g = \frac{c_P}{1 - (\omega/c_P)(\partial c_P/\partial\omega)}. \tag{11}$$

The fundamental acoustic mode propagates with approximately constant phase and group velocities approaching c_E at frequencies up to $f = 10$ MHz. Consequently, the displacements are mostly axially distributed over the fiber cross section (Fig. 1(a)). In contrast, modes propagating with low group velocities are mostly radially polarized in the fiber around $f = 30$ MHz (Fig. 1(b)). At $f = 50$ MHz, a higher order mode approaches c_E, increasing again the axial displacement distribution along the fiber. The beatlength or beat wavelength in which two modes, k_i and k_{i+1}, interfere along the fiber is expressed in terms of the modal wavenumber k as [45–47],

$$B_a = \frac{2\pi}{k_i - k_{i+1}}, \tag{12}$$

in which, i is the mode index.

For small wavelengths compared to the guide diameter, the two modes converge to the wavenumber of a Rayleigh wave k_R, with period given as,

$$B_R = \frac{2\pi}{k_R}, \tag{13}$$

in which the averaged wavenumber of the modes approaches the Rayleigh wavenumber as [46,47],

$$k_R = \frac{k_i + k_{i+1}}{2}. \tag{14}$$

Fig. 1(e) illustrates an acoustic signal induced by the beatlength of two arbitrary acoustic modes $B(1–2)$ with periods λ_1 and λ_2 evaluated at the SMF surface in Fig. 1(b) (green dashed line). The modal overlap modulates the wave amplitude distorting the signal waveform. The properties of the unrecognized mode 2 are determined by the proper characterization of λ_1 and $B(1–2)$ at the considered frequency.

The complex multimode interference in the SMF is evaluated up to $f = 80$ MHz. The wavenumbers k are computed from the roots of the Pochhammer-Chree frequency equation in Eq. (8), employing the methods and algorithms developed in Refs. [25,26,39,40]. The wavelength λ_a, phase and group velocities c_P and c_g are further derived from k. The beatlengths B_a are calculated with Eqs. (12)-(14). These parameters are named in the next sections as "Theory" and compared to the FEM simulations.

2.2. Significant acoustic parameters for modulation of optical fibers and diffractive gratings

Ultrasonic fiber sensors, such as, optoacoustic devices, are based on the phase modulation of propagating optical modes. The acoustically induced strains modulate the refractive index n and fiber length l, inducing an optical phase-shift as [17,48],

$$\Delta\beta = K_0 n \Delta l + \int_{-l/2}^{l/2} K_0 \Delta n dz, \tag{15}$$

in which, K_0 is the free-space wavenumber of the optical mode, Δl is the fiber length variation, and Δn is the change of the refractive index in the fiber core. The fiber length changes proportionally to the axially induced strain ε_z as,

$$\Delta l = \int_{-l/2}^{l/2} \varepsilon_z dz. \tag{16}$$

The sensor response is governed by the orthogonal phase-shift derived from Eq. (15) as [15,17],

$$\Delta\beta_x = 2K_0 n \int_{-l/2}^{l/2} \left[\varepsilon_z - \frac{n^2}{2}\left(p_{11}\varepsilon_x + p_{12}\left(\varepsilon_y + \varepsilon_z\right)\right)\right] dz, \tag{17}$$

$$\Delta\beta_y = 2K_0 n \int_{-l/2}^{l/2} \left[\varepsilon_z - \frac{n^2}{2}\left(p_{11}\varepsilon_y + p_{12}\left(\varepsilon_x + \varepsilon_z\right)\right)\right] dz, \tag{18}$$

where, ε_x and ε_y, are the transversal strains in the x and y axes over the fiber cross section. The coefficients of the material's strain-optic tensor are p_{11} and p_{12}. Note that the phase-shifts in Eqs. (17) and (18) are determined by the amplitude of the acoustic signal inducing the strains, as well as the fiber's material and design and the acousto-optic interaction length l.

For acousto-optic devices employing FBGs, an optical mode propagating in an unmodulated grating is reflected at the Bragg wavelength λ_B. The axially induced strain ε_z periodically modulates the mode's

effective index n_{eff} and the grating period Λ, inducing reflection bands beside the Bragg resonance $\lambda_B = 2n_{eff}\Lambda$. The normalized modulated reflectivity is written as [49],

$$\eta = \tanh^2\left[\frac{\pi\Delta n_{ac}\Gamma}{\lambda_B} l_g J_m\left(\frac{\lambda_a}{\Lambda}\varepsilon_z\right)\right], \tag{19}$$

where, Δn_{ac} and l_g are respectively the grating's index modulation amplitude and length, Γ is the optical confinement factor, and λ_a is the acoustic wavelength. J_m is the Bessel function of the first kind and order m. The separation between the modulated bands is tuned by the acoustic frequency f or period λ_a as [49],

$$\Delta\lambda = \frac{\lambda_B^2}{2n_{eff}\lambda_a}. \tag{20}$$

Axially symmetric acoustic modes have the potential to modulate standard optical fibers at frequencies higher than 10 MHz by inducing long period gratings (LPGs) [23]. Efficient coupling between the fundamental and the first higher order optical modes LP_{01} and LP_{11} at the resonant optical wavelength λ_o, occurs for the optical beatlength matching with the acoustic wavelength as,

$$\lambda_a = L_B = \frac{\lambda_o}{n_{01} - n_{11}}, \tag{21}$$

where, n_{01} and n_{11} are respectively the effective refractive indices of the modes LP_{01} and LP_{11}. The acousto-optic resonant conditions are conveniently expressed in terms of the modal beatlengths by replacing $\lambda_a = B_a$ (or B_R) in Eqs. (19)-(21). Change of the input acoustic parameters is therefore useful to tune the properties of the propagating optical modes in the fiber.

3. 2D-3D numerical experiment

3.1. Modeling the optical fiber with the finite element method (FEM)

A standard single mode optical fiber (SMF-28) is modelled by means of the Structural Mechanics Module included in the package COMSOL Multiphysics 5.4, based on the finite element method (FEM) [50]. The SMF cross section is designed as a 2D component, as illustrated in Fig. 2 (a). The fiber core and cladding diameters are respectively 8.2 μm and 125 μm. The fiber's material is defined by the silica density $\rho = 2200$ kg/m^3, Young's modulus $Y = 72.5$ GPa and Poisson's ratio $\upsilon = 0.17$ [22,27,31]. These material parameters are considered for a fiber at room temperature. Minor changes in the Poisson's ratio caused by distinct manufactures' fabrication processes or temperature fluctuations can be experimentally characterized employing the method described in Ref. [20]. The fiber cross section is meshed with triangular elements

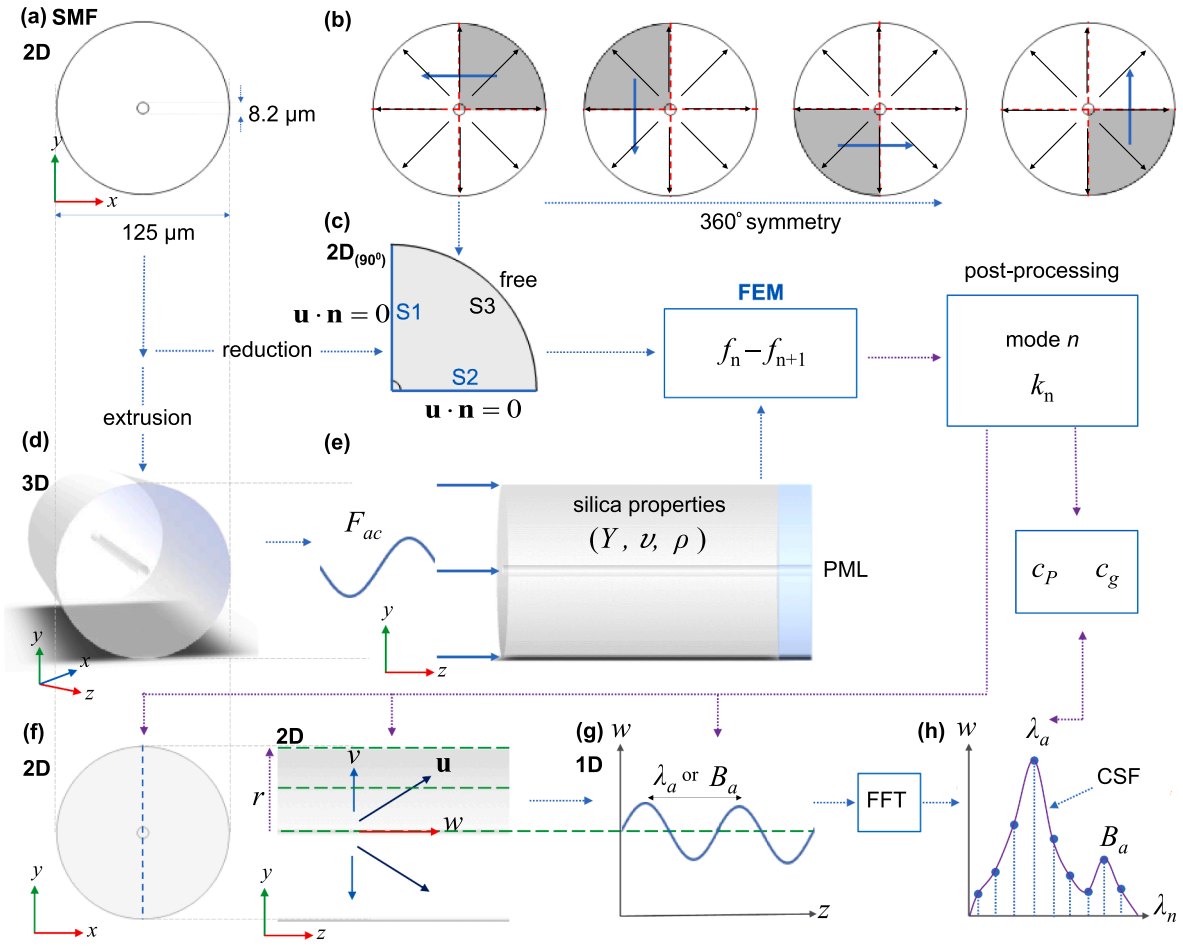

Fig. 2. Multidimensional numerical methodology to evaluate ultrasonic fields inside a standard single mode optical fiber (SMF) with the finite element method (FEM): (a) 2D SMF cross section is reduced to (b) a quarter of its size resulting in a (c) 90° symmetric geometry in relation to the x and y axes. (d) 3D solid cylinder generated from the 2D geometry. (e) Definition of the silica properties (Young's modulus Y, Poisson ratio υ and density ρ), excitation force F_{ac} and a perfectly matched layer (PML). The SMF frequency response is computed for each frequency f and the acoustically induced axial w and radial v displacements are evaluated over the (f) xy and yz fiber cross section planes. (g) The acoustic wavelengths λ_a and beatlengths B_a are characterized at the fiber surface, cladding, and core (dashed green line) and in the (h) spatial frequency spectrum by means of the fast Fourier transform (FFT). (For interpretation of the references to color in this figure legend, the reader is referred to the web version of this article.)

with a maximum element size of 0.15 μm in the fiber core and 10 μm in the cladding. The elements grow symmetrically from the fiber core to the surface with increasing rate of 1.2. The fiber boundaries are defined as a free-tension constraint. The Mode Analysis study is used to calculate the wavenumbers k and the displacement patterns of each propagating axially symmetric mode at a given frequency f, considering numerically a fiber of infinite length. The modal parameters are computed for the frequency range of $f = 1$ - 80 MHz (5 MHz steps), employing a desktop computer equipped with a 3.2 GHz Intel i7 processor (6 cores) and memory of 64 GB. The dispersion curves are further calculated in terms of k. The averaged time to compute each frequency step f is 8 s.

We have applied a modeling technique usually employed to simulate photonic devices to evaluate the acoustic modes in the SMF with a reduced computational domain [51]. The fiber cross section is split into four 90° symmetric quadrants as seen in Fig. 2(b). Fig. 2(c) shows the quadrant used to compute the modal parameters (the other quadrants are disabled). The orthogonal edges or boundaries S1 and S2 are defined as Symmetry Plane nodes, indicating a symmetric geometry to both orthogonal x and y fiber axes (red dashed lines in Fig. 2(b)). The constraint, $\mathbf{u} \cdot \mathbf{n} = 0$, indicates that displacements normal to the boundaries S1 and S2 are null ($\mathbf{u}$ is a radial vector parallel to the axes x and y, and $\mathbf{n}$ is the unit vector perpendicular to $\mathbf{u}$). S3 is set as a free-tension constraint. Consequently, only axially symmetric modes composed of radial and axial vector components are computed. This approach benefits the use of the same fiber design, material and mesh employed in Fig. 2(a), reducing the model's size, computing requirements and solution time. The wavenumbers k are computed with a high frequency resolution of 20 kHz from $f = 20$ kHz to 80 MHz, employing the same desktop computer. The averaged time to compute each frequency step f is 3 s.

The 2D fiber geometry in Fig. 2(a) is extruded along 1 cm to generate a 3D solid cylinder (Fig. 2(d)). A sinusoidal force with constant amplitude of $F_{ac} = 3 \times 10^{-3}$ N is axially applied at the fiber end from $f = 10$ to 80 MHz (1 MHz step), as illustrated in Fig. 2(e). A perfectly matched layer (PML) of 100 μm in thickness is set at the other fiber end as an absorbing boundary condition [50]. The PML prevents the reflection of the propagating modes in the fiber by strongly absorbing the waves at the ending interface. The remaining fiber surfaces are set as a free-tension constraint. The SMF cross section is meshed at the 2D xy plane ($z = 0$) with triangular elements with a maximum element size of 6 μm. The elements increase symmetrically from the fiber core to the surface with the rate of 1.2. The 2D mesh is extruded along the fiber in steps of 5 μm in thickness, resulting in 2000 layers in the fiber length and 20 layers in the PML. The maximum averaged element size is about 8 times smaller than the shortest acoustic wavelength of $\lambda_R = 43$ μm, calculated with Eq. (10) at 80 MHz. It provides high spatial resolution to evaluate the wavelengths and beatlengths in the considered frequency range, satisfying the element size requirements for accurate FEM computation [50]. The fiber's frequency response is computed for each frequency step f. The Cluster Sweep function is employed to configure each step f as a "job", which is computed by 14 cluster nodes (each one equipped with 28 processor-cores and 128 GB memory). The considered frequency range is distributed and solved in parallel by means of 2000 processor-cores and 9 TB of memory, provided by the high-performance computer center HPC Midlands Plus. The averaged time to compute each frequency step f is 7 min.

The acoustically induced displacements are decomposed into axial w and radial v components evaluated at the fiber surface ($r = 62.5$ μm) and cladding mid radius ($r = 31.25$ μm), as indicated by the green dashed lines in Fig. 2(f). Only the axial components are evaluated at the fiber core center ($r = 0$) because the resulting vector of symmetric radial components is ideally null at this position [22]. It allows the characterization of the 3D complex waveforms caused by the modal interference employing a 1D wave sample of the symmetric displacement distribution over the xy geometry. A wavelength λ_a or beatlength B_a in the fiber core is illustrated in Fig. 2(g). The dispersion spectrum of the n modes supported by the SMF (Fig. 2(h)) is computed at the considered radial positions by means of the peak-to-peak method and the fast Fourier transform (FFT). The FFT spectrum is fitted with a cubic spline interpolation function (CSF) as described in the next section.

3.2. Modal decomposition and spectral evaluation of complex ultrasonic fields in the optical fiber

The mode's wavelengths λ_a and beatlengths B_a are simultaneously computed by means of the fast Fourier transform (FFT) [45,46]. The FFT converts the acoustic signal in the spatial domain to the frequency domain ($f_z = z^{-1}$) [46]. The simulated radial and axial displacement modulus $|v|$ and $|w|$ are sampled along the z-axis with a spatial resolution of Δz (μm), totaling N samples along the fiber length. The sampling frequency is calculated as, $F_s = \Delta z^{-1}$ (μm^{-1}), resulting in the resolution of $\Delta f_z = F_s N^{-1}$ (μm^{-1}), which is expressed in terms of Δz as [52,53],

$$\Delta f_z = \frac{1}{N \Delta z}. \tag{22}$$

The samples in the FFT spectrum are $0.5N$. The acoustic period $\lambda_a(z)$ is calculated from the inverse values of the spatial frequency f_z as,

$$\lambda_a(j) = 2 \sum_{j=1}^{j=\frac{N}{2}+1} \frac{1}{f_z(j)}, \tag{23}$$

where, j is the frequency component index. Fig. 2(h) illustrates the FFT modulus of axial displacements (blue solid circles). The wavelengths λ_a and beatlengths B_a are measured at the peak's position in the spectrum. The distance between consecutive spectral λ_a points is given as,

$$\Delta\lambda_a(j) = \lambda_a(j) \frac{1}{j}, \tag{24}$$

for $j = 1$ to $0.5N + 1$. Consequently, increasing the number of samples N can improve both spatial frequency Δf_z and wavelength $\Delta\lambda_a$ resolution. $\Delta\lambda_a$ is significantly improved by fitting the FFT spectrum with a cubic spline interpolation function (CSF) (solid curve in Fig. 2(h)) [53]. It provides a constant resolution of $\Delta\lambda_a = 0.1$ μm for the whole FFT spectrum, increasing the accuracy to measure the peak's location. The dispersion curves are evaluated from the FFT spectra for the frequency range of $f = 10 - 80$ MHz.

The modal dispersion is also computed with the averaged peak-to-peak method (APP) [38]. The wavelength λ_a is calculated by measuring the distance between the nodes and peaks of the standing acoustic wave and averaging a sequence of $1/4\lambda_a$ wavelengths. The APP method is accurate to measure waves with low amplitude discrepancies between consecutive peaks, since large amplitude modulation might affect the peak's location. The method is robust for period variations along the fiber length, which are compensated by the averaging process. Overall, APP's accuracy increases for waves approaching constant period and amplitude.

4. 2D vibration patterns and dispersion of the acoustic modes in the SMF

The frequency-dependent variation of the modal wavenumber k, wavelength λ_a, phase c_P or group c_g velocities is useful to study the polarization and distribution of the acoustic modes over the fiber cross section. The acoustic parameters provide information about the nature of the beatlengths and resonances, which are essential to predict the modulated optical properties, as discussed in Section 2.2. In this section, we show the vibration patterns and dispersion curves of the acoustic modes supported by the SMF computed with the 2D geometries modelled in Section 3.1.

Fig. 3(a) shows the variation of the wavenumbers k of the fundamental acoustic mode $L(0,1)$, second and third higher order modes L

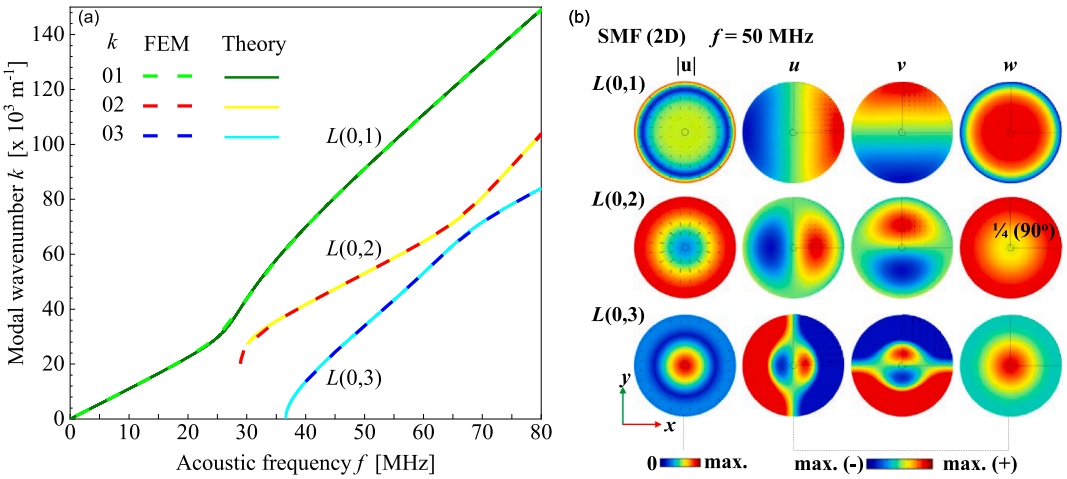

Fig. 3. (a) Dispersion of the wavenumbers k of the fundamental mode $L(0,1)$ and higher order acoustic modes $L(0,2)$ and $L(0,3)$ in the SMF up to $f = 80$ MHz. The FEM simulated curves (dashed lines) are compared to the theoretical reference values (solid lines). (b) 2D FEM simulated displacement distribution $|\mathbf{u}|$ of $L(0,1)$, $L(0,2)$ and $L(0,3)$ over the SMF cross section at $f = 50$ MHz. The displacements are decomposed into the radial components v and u (polarized respectively in the y and x axes) and the axial component w. The SMF cross section is compared to the 2D 90° reduced-domain symmetric geometry. The black arrows indicate the distribution of the radial components for each polarization.

(0,2) and $L(0,3)$ up to $f = 80$ MHz. The FEM simulated dispersion curves (dashed lines) are compared to the values calculated with the Pochhammer-Chree frequency equation in Eq. (8) (solid curves). The overall averaged agreement between the curves is 99.9 %. Fig. 3(b) shows respectively the simulated displacement distribution of $L(0,1)$, $L(0,2)$ and $L(0,3)$ over the SMF cross section at $f = 50$ MHz. The color of $|\mathbf{u}|$ is normalized to the maximum (red color). The displacements are decomposed into the radial components v and u (respectively polarized in the y and x axes) and the axial component w, normalized to the maximum negative (dark blue color) and positive (dark red color). The black arrows indicate the distribution of the radial components for each polarization.

The SMF cross section is overlapped with the 90° reduced-domain symmetric geometry for comparison. The $|\mathbf{u}|$ distribution of $L(0,1)$ and $L(0,3)$ contains wave nodes over the fiber cross section. The absence of nulls over the axial distribution of $L(0,2)$ shows that the second higher order mode propagates predominantly as a longitudinal acoustic wave at the considered frequency. Meanwhile, high $|\mathbf{u}|$ concentration of $L(0,1)$ over the fiber surface indicates its tendency to propagate as Rayleigh waves with increasing frequency. In contrast, high axial distribution of $L(0,3)$ is noted over the fiber core. The similar pattern of the displacement fields $|\mathbf{u}|$ and w indicates that the axial displacements are dominant over the fiber cross section.

Fig. 4(a)-(c) show respectively the FEM simulated displacement distribution of the acoustic modes $L(0,1)$, $L(0,2)$, and $L(0,3)$ over the SMF cross section up to $f = 80$ MHz (5 MHz steps). The displacement modulus colors are normalized to the maximum of the first sample at $f = 1$ MHz (dark red color). The simulated dispersion curves are computed with the 2D 90° reduced-domain symmetric geometry and compared to the Pochhammer-Chree reference curves in Fig. 4(d). The phase and group velocities are derived from k with $c_P = 2\pi f k^{-1}$ and $c_g = \partial k/\partial\omega$. The dilatational c_D, transversal c_T and Rayleigh c_R velocities (dotted black lines) are respectively calculated with Eqs. (3), (4) and (10) and included as references in Fig. 4(d). The velocities are normalized to the extensional material velocity c_E in Eq. (9), as indicated with c_{rel}. The averaged agreement between the simulated and analytical curves is 99.9 %.

Note in Fig. 4(d) that the phase and group velocities of the fundamental acoustic mode $L(0,1)$ are nearly constant for the low dispersive range up to $f = 10$ MHz, approaching the extensional velocity as, $c_g \sim c_P \sim c_E = f\lambda_a$. The acoustic period λ_a is easily determined in this range at any given frequency f. Nevertheless, increasing frequency induces a non-linear velocity response and high radial polarization of $L(0,1)$ and $L(0,2)$ in Fig. 4(a) and 4(b). High confinement of these modes overlapping with close group velocities over the fiber cross section induces a strong radial resonance at this frequency. Similarly, a second resonance induced by the interference of $L(0,2)$ and $L(0,3)$ propagating with similar group velocities is noted at $f = 68$ MHz. The vibration patterns of these modes at close resonant frequencies indicate increased concentration of axial displacements in the fiber core, where $L(0,3)$ is mostly distributed.

The fundamental mode becomes increasingly concentrated over the fiber surface from $f = 50$ MHz, approaching the velocity of dispersionless Rayleigh waves c_R with increasing frequency. The velocity of $L(0,2)$ approaching c_E denotes the formation of longitudinal plane waves along the fiber. It is also expected for $L(0,3)$ at frequencies higher than $f = 80$ MHz, repeating the dominance cycle with the emergence of other higher order modes. In general, the modal properties considerably change in a non-linear response with frequency. Accordingly, the vibration patterns of the modes change from radial to axial displacement distribution and polarization over the fiber cross section. The dispersion curves are useful to study the independent propagation of axially symmetric modes in optical fibers, regardless of the fiber length or acoustic power applied at the fiber end. The discrete number of supported modes and their spatial distribution depend only on the fiber geometry, material, and excitation frequency. For practical purposes, the dispersion curves are equally important to calculate the waveguide impedances required to match acoustic transmitters, receivers or layers attached on the fiber surface [41]. The full characterization of the modal interference and resonances requires the simultaneous excitation of the modes to interact along the fiber. This is achieved by carrying out a frequency response of the 3D FEM simulations of the SMF discussed in the next section.

5. 3D spatial-spectral evaluation of the propagating acoustic modes and beatlengths in the SMF

The FEM simulated multimode interference, beatlengths and resonances are characterized along the optical fiber with the FFT and APP methods described in Section 3.2. The modal dispersion curves are provided simultaneously in the 2D FFT spectrum in Fig. 5 in terms of the acoustic period for the frequency range from $f = 10$ to 80 MHz. The FFT spectra are normalized to the maximum displacement modulus (yellow color) and compared to the APP method (black line). The simulated variation of the modes' wavelengths λ_a and beatlengths B_a is compared to the values calculated with the Pochhammer-Chree frequency equation (Eq. (8)) with an overall averaged accuracy of 99.9 %. The

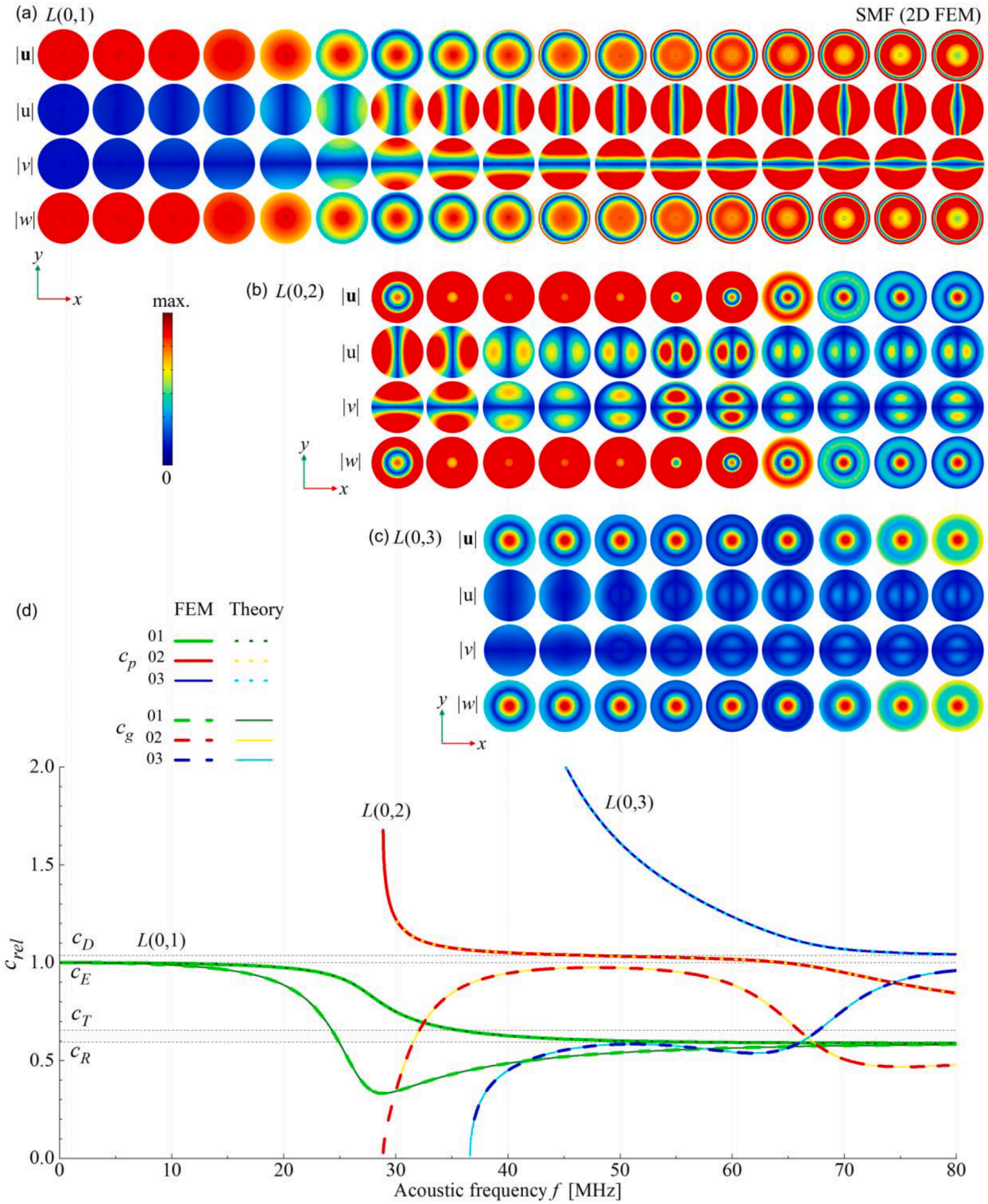

Fig. 4. 2D FEM simulation of the vibration patterns of the (a) fundamental acoustic mode $L(0,1)$, (b) second higher order mode $L(0,2)$, and (c) third higher order mode $L(0,3)$ in the SMF. The displacements are decomposed into radial (v and u) and axial (w) components. (d) Dispersion curves of the phase and group velocities c_P and c_g of the modes for frequencies up to $f = 80$ MHz. The simulated curves are compared to the theoretical reference values.

beatlengths of the modes, $L(0,1)$ - $L(0,2)$, and, $L(0,2)$ - $L(0,3)$, overlapping as Rayleigh waves are indicated respectively as, $B_R(1–2)$ and $B_R(2–3)$. Second order harmonics are indicated as, $B_2(1–2)$ and $B_2(2–3)$.

Fig. 5(a) shows the spectrum of the axial displacements at the fiber surface. $L(0,1)$ superimposes with the emergent second order mode $L(0,2)$ inducing a strong resonance in the SMF around $f = 29$ MHz. It is followed by the rising beat $B_2(1–2)$. At higher frequencies, increasing dominance of $L(0,2)$ contributes to the generation of longitudinal plane waves along the fiber up to $f = 65$ MHz (note that the APP curves overlap with the period of $L(0,2)$). The dominant mode propagates with velocities significantly higher compared to the other modes, approaching the extensional material velocity c_E (Fig. 4(d)). Consequently, the beatlengths are reduced in the range of high modal dominance around $f = 40 – 60$ MHz. Afterwards, $L(0,2)$ propagates with decaying velocities

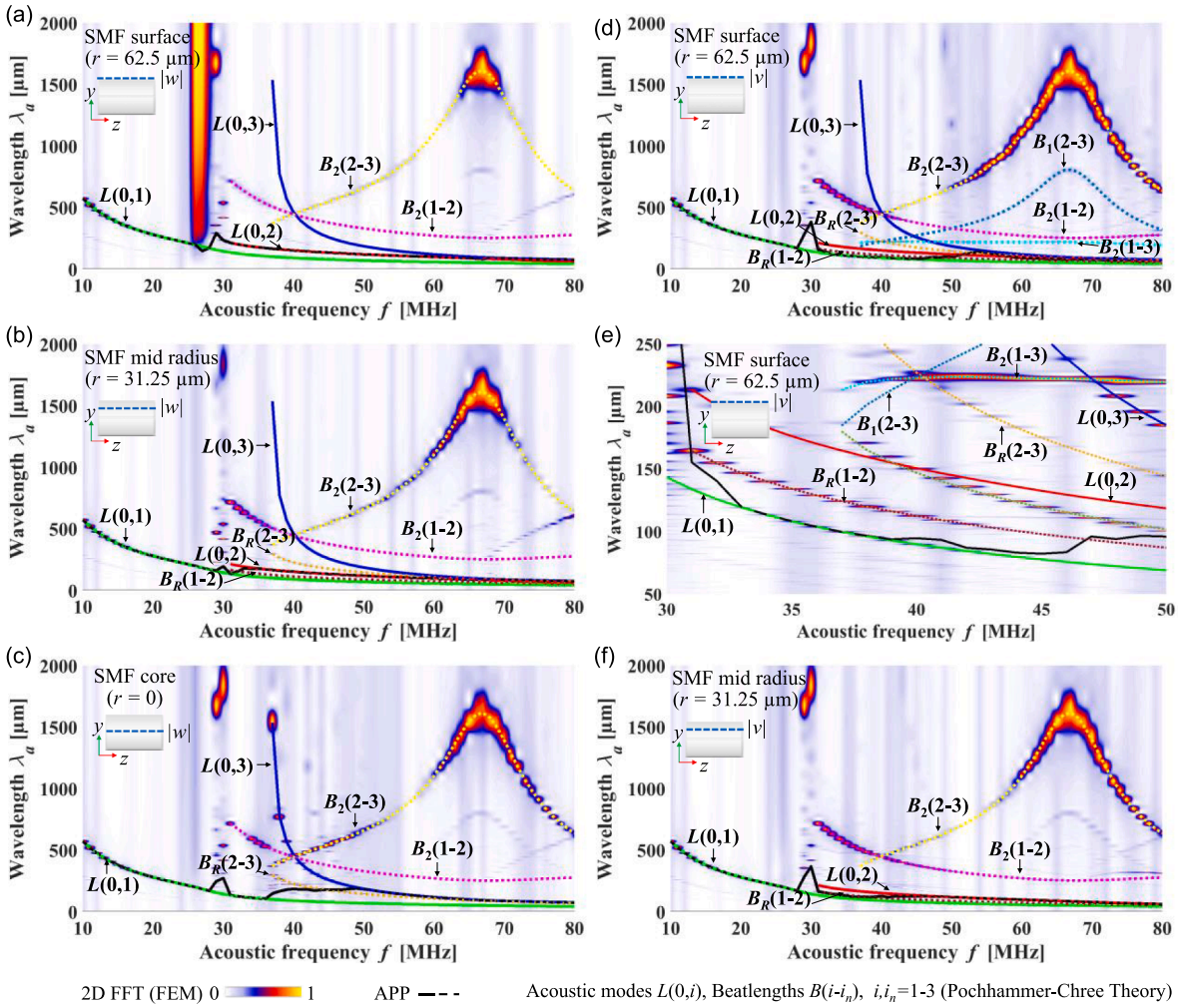

Fig. 5. 2D FFT spectra of the FEM simulated axial displacements $|w|$ at the SMF (a) surface, (b) cladding and (c) core for the frequency range of $f = 10$ - 80 MHz. Spectra of the radial displacements $|v|$ at the (d) fiber surface and (f) cladding. (e) Detail of the beatlengths at the fiber surface in the range of $f = 30 – 50$ MHz. The dispersion curves show the variation of the wavelengths λ_a of each acoustic mode (solid lines) and induced beatlengths B_a (dotted lines) calculated with the Pochhammer-Chree frequency equation. The FFT spectra are compared to the APP method (black line).

toward Rayleigh waves with increasing frequency. Converging velocities of $L(0,2)$ and $L(0,3)$ reinforce the beats $B_R(2–3)$ and $B_2(2–3)$, achieving maximum interference at the resonance of $f = 68$ MHz.

The beatlengths are emphasized in the spectrum of the axial components in the fiber cladding ($r = 31.25$ μm) in Fig. 5(b). The beats $B_R(1–2)$ and $B_2(1–2)$ are strengthened near the first resonant band, indicating a transition range exchanging the periods of $L(0,1)$ and $L(0,2)$. From $f = 37$ MHz, $L(0,2)$ expands the axial field over the fiber cladding and surface, polarizing along the fiber length (note the similar period responses of $L(0,2)$ in Fig. 5(a) and 5(b)). Nevertheless, it is not observed in the spectrum of the axial displacements at the fiber core ($r = 0$) in Fig. 5(c). Stronger interaction of $L(0,2)$ and $L(0,3)$ strengthens the beats $B_R(2–3)$ and $B_2(2–3)$. $B_R(2–3)$ contributes to increase the period of the propagating acoustic waves up to $f = 50$ MHz, further reducing it around the second resonant peak (the APP curve approaches $B_R(2–3)$ in the transition range between periods of $L(0,1)$ and $L(0,3)$). At the remaining frequencies, the overlapped FFT-APP curves indicate high concentration of $L(0,3)$ in the fiber core. The second resonant band is governed by the beats $B_R(2–3)$ and $B_2(2–3)$ around $f = 68$ MHz.

The dispersion of the radial components at fiber surface is shown in Fig. 5(d). Note that the beatlengths are significantly reinforced in the resonant bands, mainly $B_2(1–2)$ and $B_2(2–3)$ compared to the spectra of the axial components in the fiber. Fig. 5(e) shows details of the dispersion curves in the range of $f = 30 – 50$ MHz. The APP curve indicates increased concentration of the fundamental mode at the fiber surface interacting with the higher order modes by means of $B_R(1–2)$, $B_2(1–2)$ and $B_2(1–3)$. Similarly, overlapped radial components of the higher order modes significantly strengthen $B_R(2–3)$ and $B_2(2–3)$. The intense modal interaction at the fiber surface also contributes to enhance new harmonics in the spectrum, such as, $B_2(1–3)$ and $B_1(2–3)$. It is because the high radial polarization of the modes at the resonances. In addition, the guide surface is a common reflection interface for all the propagating modes. The multimode interference reciprocally transfers energy between the fiber surface and core center according to the beatlengths, achieving maximum confinement in the fiber core at the resonances. The modal interaction is reduced at the cladding mid radius in Fig. 5(f) because the concentration of the dominant mode $L(0,2)$.

In summary, the fundamental mode $L(0,1)$ is dominant and highly distributed over the fiber cross section up to about $f = 28$ MHz. The resonant bands with peaks at $f = 29$ MHz and $f = 68$ MHz are emphasized in all spectra in Fig. 5, showing that the resonances are composed of both radial and axial components highly confined over the fiber cross section. Radial or transversal polarization is predominant at the first resonant peak, considering high overlapping of the modes approaching the transversal and Rayleigh velocities, c_T and c_R. The FEM simulated dispersion curves provide a graphical and intuitive tool to investigate the modal interference and resulting beatlengths, changing considerably the displacement distribution over the SMF cross section with increasing

frequency. The acoustic period λ_a is directly estimated at any specific region in the fiber and given frequency f in the spectrum, which is useful to evaluate the modulation of FBGs and LPGs discussed in Section 2.2. Furthermore, other acoustic parameters, such as, wavenumber k, phase and group velocities, c_P and c_g, can be directly derived from the FFT spectra. The frequency-tunable redistribution of the modes has potential to spatially switch the acoustic energy between the fiber surface, cladding, and core, offering promising possibilities to convert and filter the acoustic modes as discussed in Section 7.

6. Analysis of the acoustic resonances, modal dominance, and induced strains inside the optical fiber

6.1. Modal dominance and displacement distribution in the SMF

The dominance of the acoustic modes in the SMF is investigated employing the information derived from the FFT spectra in Section 5. Fig. 6(a) shows the ratio between the axial displacements w and the overall displacements integrated over the SMF cross section along the fiber length (black curve). The highest magnitude levels around $f = 10$ MHz, $f = 50$ MHz and $f = 80$ MHz indicate respectively the ranges of dominance of the fundamental $L(0,1)$ and higher order modes $L(0,2)$ and $L(0,3)$. The modes propagate with group velocities approaching the extensional material velocity c_E at these frequencies. Consequently, the axial displacements of a dominant mode are mostly in phase over the fiber cross section. The notches in the displacement response therefore correspond to the highest concentration of radial components in the fiber.

The fraction of the axial components in the fiber core (red curve) is compared to the frequency range of the beatlengths $B_2(1–2)$ and $B_2(2–3)$. Note that the displacement peaks have high correlation with the beats and resonances previously shown in the FFT spectra. The resonant bands correspond to the transition ranges of modal dominance. The bandwidth and slope of the resonances highly agree with the range and slope of the considered beats. The first resonant band coincides with the frequencies in which the fundamental mode achieves the lowest group velocities. Consequently, increased distribution of radial components over the fiber cladding and surface induces axial components in the fiber core. The interaction of $L(0,2)$ with $L(0,3)$ gradually enhances the axial distribution in the fiber core, reaching a maximum with decreasing group velocity of $L(0,2)$ at $f = 68$ MHz.

Fig. 6(b)(f)(j) show the 3D FEM simulation of the SMF exemplifying the dominance of the acoustic modes $L(0,1)$, $L(0,2)$ and $L(0,3)$ respectively at $f = 10$, 50 and 80 MHz. Details of the acoustic waves propagating inside the fiber are shown in the 2D cross section planes. Fig. 6(c)(g)(l) show the ultrasonic fields over the yz fiber cross section along 1 mm. The displacement modulus $|\mathbf{u}|$ is decomposed into the radial v and axial w components (normalized to the maximum positive (dark red color) and negative (dark blue color)). The agreement between the vibration patterns of $|\mathbf{u}|$ and w confirms qualitatively the highest concentration of axial components inside the fiber, as seen in Fig. 6(a). The vibration pattern of each mode is identified from the displacements over the xy cross section. Fig. 6(d)(h)(m) show the 2D modal patterns extracted from the 3D simulation (dashed black lines in the yz cross sections) compared to those obtained from the 2D modal analysis in Fig. 6(e)(i)(n) (Section 4). The comparison of the two independent 3D and 2D techniques indicates good qualitative agreement of the modal distribution in the SMF.

At $f = 10$ MHz, the single-mode acoustic propagation in a low dispersive range induces well defined longitudinal acoustic waves uniformly distributed along the fiber. The sinusoidal periodic waveforms of both axial and radial components of the fundamental mode $L(0,1)$ are 90° out-of-phase along the fiber in Fig. 6(c). Distortion of the waveform is however evident at $f = 50$ MHz in Fig. 6(g). The characterization of the

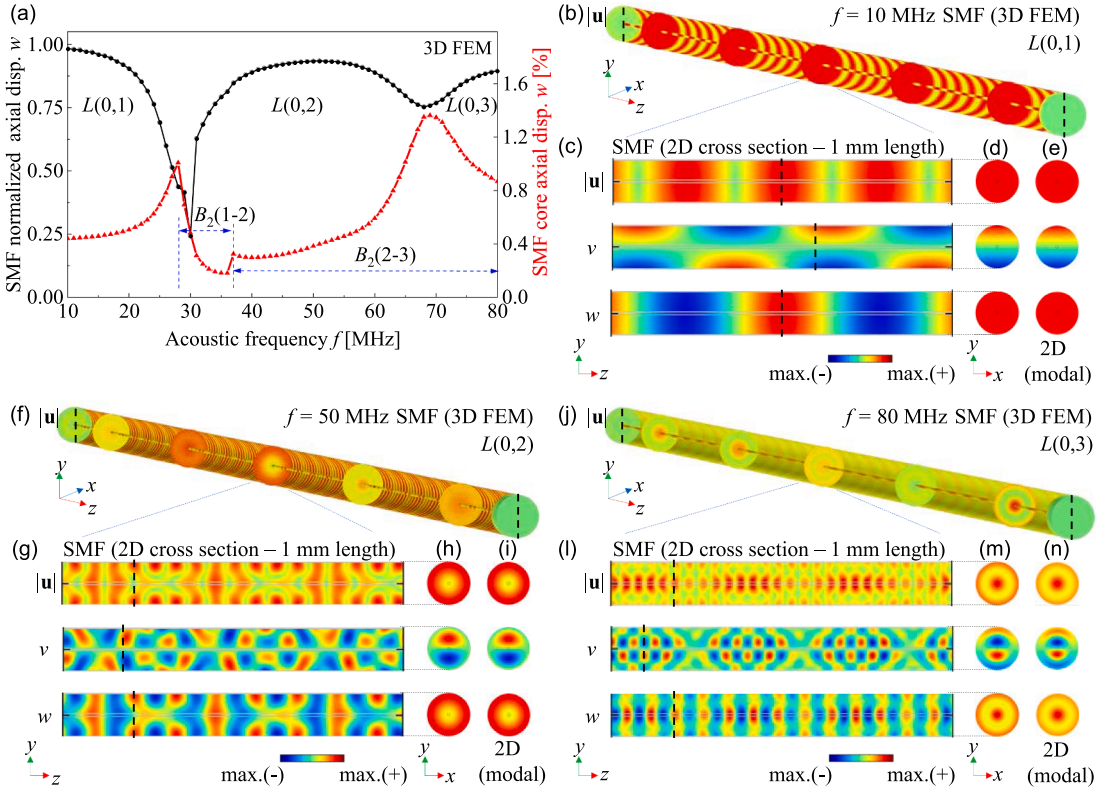

Fig. 6. (a) Normalized axial displacements integrated over the SMF cross section (black curve) and fiber core (red curve). The peaks indicate resonant concentration in the fiber core caused by the beatlengths $B_2(1–2)$ and $B_2(2–3)$. The dominance of the acoustic modes inside the SMF is exemplified by the 3D/2D FEM simulations at the frequencies of (b)-(e) $f = 10$ MHz, (f)-(i) $f = 50$ MHz, and (j)-(n) $f = 80$ MHz, in which the axial displacements are mostly distributed over the fiber cross section. (For interpretation of the references to color in this figure legend, the reader is referred to the web version of this article.)

superposed modal fields is performed by evaluating the displacement components. $L(0,2)$ is identified by inducing longitudinal planes along the fiber. Coupling of $L(0,1)$ and $L(0,3)$ cause high distortion of the acoustic fields in the fiber surface and core. At $f = 80$ MHz, the modes overlap with close wavelengths, contributing to create again plane waves along the fiber, as shown by the axial components w in Fig. 6(l). $L(0,3)$ is predominant in the fiber cross section, as seen in Fig. 6(m) and 6(n). A periodic modulation of the radial fields v by the beatlengths is noted in Fig. 6(l). The modal superposition reinforces the displacements of the dominant mode $L(0,3)$ in the fiber core. The modes' period at the fiber surface, cladding and core are determined in the FFT spectra at the considered frequencies, providing a complete set of information to quantify the acoustic fields inside the fiber.

6.2. Beatlength-induced resonances and strains in the SMF core

Attenuation and distortion of acoustic signals at high frequencies restrict the pulse repetition rate of acoustically modulated fiber lasers mode-locked at twice the acoustic frequency. Similarly, optoacoustic sensors operating with signals as broad as 80 MHz exhibit significantly reduced sensitivity and image distortions caused by resonances around 22 - 30 MHz and 70 - 80 MHz, separated by a high attenuation range from 40 to 60 MHz [15]. In addition, coupling of acoustic waves with relevant distinct velocities in the fiber induces image artifacts. Evaluation of these resonant bands in a wide frequency range may be useful to enhance the sensitivity and spatial resolution required to reconstruct reliable images.

In this section, we show that the resonances investigated in current fiber-optic sensors are partially caused by the interference of propagating axially symmetric acoustic modes inducing beatlengths. As previously discussed in Section 6.1, the frequency response of the acoustic waves in the fiber core is significantly different from the response of the overall fiber cross section. In the FEM simulations, the ultrasonic fields are ideally composed of equivalent orthogonal strain components ε_x and ε_y over the SMF cross section. These strains and the axial strain ε_z are integrated along the fiber core for the range of $f = 10$ - 80 MHz. Fig. 7 shows the frequency response of the strains in the fiber core, indicating the resonances and beatlengths induced by the multimode interaction. As observed in experimental devices, the first resonant band has a peak at $f = 29$ MHz [16]. Note that the radial components abruptly increase towards the peak. The resonant coupling of $L(0,1)$ and $L(0,2)$ is gradually reduced with increasing axial polarization of $L(0,2)$, weakening the beat $B_2(1–2)$. It is followed by stronger interaction of the higher order modes from $f = 37$ MHz. The strain components further increase according to $B_2(2–3)$, achieving a maximum at the second resonance peak

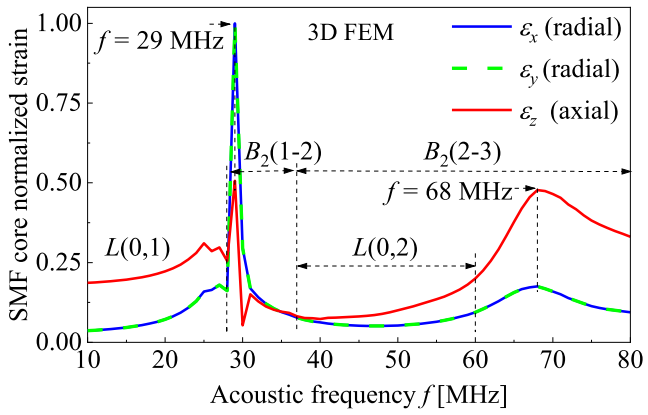

Fig. 7. FEM simulated frequency response of the acoustically induced radial ε_x, ε_y and axial ε_z strains in the SMF core for the frequency range of $f = 10 – 80$ MHz. The resonant bands are mostly defined by the beatlengths between the fundamental and higher order modes $B_2(1–2)$ and $B_2(2–3)$.

of $f = 68$ MHz. The frequency range of high strain attenuation between the resonances coincides with the dominance band of $L(0,2)$, reducing the beats and induced strains. The simulated resonance peaks agree with experimental measurements reported in Refs. [15,16,18] (even smaller peaks on the left side of the first peak are perceived). Although birefringence and additional excitation of torsional or circumferential modes can induce other peaks at frequencies around $f = 20$ MHz, the second peak is predominant over $f = 70$ MHz [15,18]. It indicates that axially symmetric multimode interference has a significant contribution in the response of the reported optoacoustic devices.

Fig. 8(a) shows the 3D FEM simulation of the acoustically induced strains inside the SMF at the resonance peak of $f = 29$ MHz, with a detail of the yz fiber cross section along 2 mm in Fig. 8(b). The volumetric strain ε_V is decomposed into radial and axial components in Fig. 8(c) and 8(d). The modes $L(0,1)$ and $L(0,2)$ overlap radially polarized over the fiber cross section at the resonance. This modal interaction weakens with increasing difference of the modes' group velocities and emergence of $L(0,3)$. The 3D/2D strain distributions induced at the second resonance are shown respectively in Fig. 8(e) and 8(f). The superposition of the higher order modes by means of $B_R(2–3)$ and $B_2(2–3)$ contributes to exchange of acoustic energy from the fiber surface to the core. This energy redistribution in the SMF is analogous to the beatlength resonances investigated in ultrasonic plates, reflecting periodically energy between the opposite sides of the plates [45–47]. The fundamental and second higher order modes tend to concentrate as Rayleigh waves on the fiber surface for frequencies higher than 80 MHz. Meanwhile, $L(0,3)$ axially polarizes in the fiber, attenuating again the strain distribution in the fiber core with increasing frequency. The emergence of new higher order modes is also expected. Overall, the results show that the natural acoustic resonances in the optical fiber are strongly dependent on the guide material and geometry. Changes in the cross-section design, diameter and composition may possibly be used to adjust the modal beatlengths, enabling possibilities to improve the sensor's sensitivity towards a flat response over a broadband frequency range, as discussed in the next section.

Previous analytical studies show that a solid silica fiber can support axially symmetric (longitudinal) and non-symmetric (flexural and torsional) acoustic modes [22]. Flexural modes become highly weak or even inexistent with increasing frequency from 10 MHz, since the decreasing acoustic wavelength approaching the fiber diameter is unable to produce relevant curvatures in the fiber. In contrast, torsional or circumferential modes can be excited along a SMF by applying a localized force laterally distributed over the fiber surface. It is achieved by exposing the fiber surface to spherical acoustic waves [15,17]. The obliquely incident waves produce both transverse and axial strains in the fiber, inducing simultaneously longitudinal and torsional modes which do not fully interfere over the fiber cross section [48]. Therefore, co-propagating torsional modes would induce additional peaks around 20, 40 and 80 MHz in the spectrum of Fig. 7 [15,17]. The agreement between the simulated resonances around 29 and 68 MHz in Fig. 7 with previous experiments shows that the axially symmetric modes are predominant in comparison to the torsional modes even considering a lateral excitation [15,16]. The axial excitation employed in our study shows a promising alternative to emphasize only the propagation of symmetric modes inducing higher axial strains in the fiber core. It efficiently modulates the optical phase and grating properties as discussed in Section 2. Alternative setups producing similar results would consider the symmetric radial excitation of the fiber as demonstrated in Ref. [16].

7. Results discussion and outlook for the development of fiber-optic ultrasonic devices

This section discusses the main contributions provided by this numerical study, indicating how the findings, methods and simulations can further be applied and advanced to improve current fiber-based devices. A route for the development of new all-fiber acousto-optic modulators

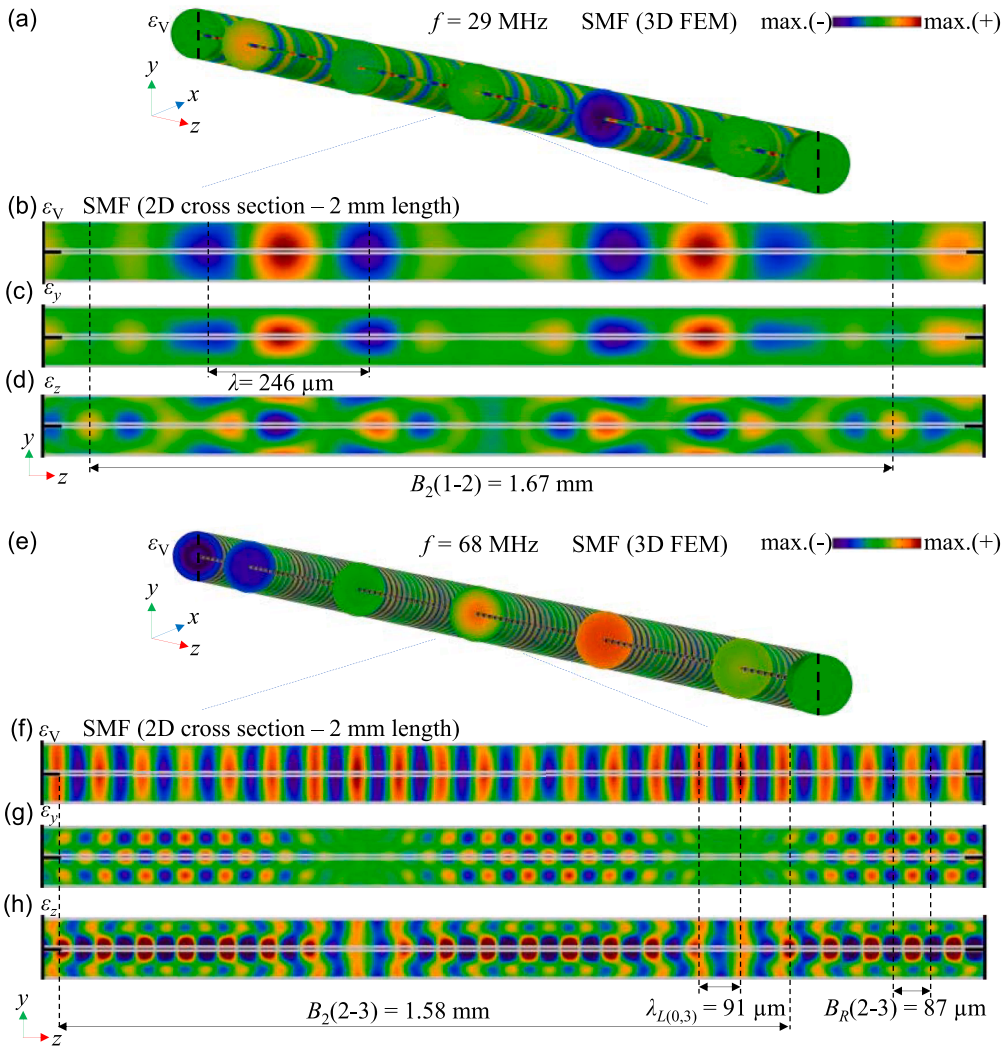

Fig. 8. 3D FEM simulation of the axially symmetric acoustic resonances at (a) f = 29 MHz and (e) f = 68 MHz. The strain distribution on the (b)(f) SMF yz cross section is decomposed into (c)(g) radial and (d)(h) axial components.

and fiber sensors is described.

1) Modal decomposition from complex ultrasonic fields inside the optical fibers: The demonstrated 3D and 2D FEM-based methods provide an efficient tool to investigate distorted ultrasonic fields over the fiber cross section by means of a modal interference method. 2D 90° reduced-domain modal analysis reduces about 63 % the computing time to calculate the modes' vibration patterns and parameters compared to the entire 2D fiber geometry. The 3D simulated frequency response shows details of the induced displacements and strains inside the fiber, which are useful to evaluate the acousto-optic interaction in the fiber core. Modeling of angle-dependent acoustic sources employed in opto-acoustic devices may be implemented by changing the boundary conditions in Section 3.1. Thus, fiber coatings and sensing substances surrounding the fiber might be integrated by adding the component geometries, materials and physical domains [4,19,34]. Variations in the resonances caused by defects in the fiber geometry or use of different materials can be predicted and directly evaluated in the FFT spectra. FEM can be efficiently employed to simulate complex multiphysics interactions, e.g., between acoustic and optical properties in the fiber core [4,19]. Photonic crystal fibers and microstructured optical fibers with complex geometries can also be modelled employing the proposed methodology [1].

2) Numerical investigation of axially symmetric resonances in fiber-optic ultrasonic devices: the nature of broadband ultrasonic resonances in optical fibers is investigated here with the finite element method for the first time. The resonant bands currently define the frequency ranges of high sensitivity and attenuation of practical devices, causing image distortions in optoacoustic sensors. This numerical study provides the following findings and conclusions about the resonances:

(a) Modes: the fiber supports a discrete number of modes changing with frequency. Each mode has a unique wavenumber k and displacement pattern (2D modeling in Fig. 3). The modes constitute the fundamental mechanism in the resonances' generation. The polarization of the acoustic modes is associated with the orientation and distribution of their vector components over the waveguide cross section. All the investigated axially symmetric acoustic modes have only radial and axial vector components [35,36]. Consequently, these modes have the same vectors' orientation and polarization. Interference between these modes can be considered as a constructive and destructive sum of the modes' vector components over the cross section and along the fiber. Although these modes can assume distinct velocities and vector magnitudes tending to a mostly radial or axial polarization at certain frequencies, the polarizations of these acoustic modes are not orthogonal. Wavenumbers k of two acoustic modes propagating in the fiber converge to close values at the resonances of f = 29 and 68 MHz (Fig. 3(a));

(b) The modal displacement fields are resonant and strongly radially polarized within the fiber cross section (Fig. 4(a)-4(c));

(c) Modes propagating with similar group velocities approaching the

transversal and Rayleigh velocities, c_T and c_R, interfere in phase at the resonances (Fig. 4(d));

(d) Beatlengths: constructive and destructive interference is caused by the phase velocity difference between the different modes inducing beating effects [54]. The beatlength is the spatial measure or period between two maxima or minima of the modal interference. It might be experimentally characterized by measuring the distance between two consecutive displacement peaks on the fiber surface [45–47]. The FFTs in Fig. 5 measure theses peaks numerically in both radial and axial displacements along the fiber. The agreement between the analytical and simulated shows the high accuracy of the results. The terms "exchange" and "transfer" are usually employed to express the redistribution of the overlapped displacements (or energy) in a waveguide cross section caused by modal interference [43–45]. Consequently, the displacement or strain redistribution is also periodic along the SMF with the beatlengths, which are evaluated from both radial and axial displacements in Fig. 5. The FFT spectra of the ultrasonic fields reveal that the resonances are caused by beatlengths induced by the modal interference, exchanging periodically acoustic energy between the fiber surface, cladding, and core (Fig. 5). The first resonance emerges from the interaction of the fundamental and second order mode by means of B_R(1–2) and B_2(1–2). The second resonance is induced by the beats of the higher order modes B_R(2–3) and B_2(2–3);

(e) The resonant frequency bands correspond to the transition ranges between the dominance bands of the modes. In the dominance frequencies, modal interaction in the fiber core is significantly reduced, causing attenuation bands in the strain spectrum, such as, from 40 to 60 MHz (Fig. 7). The dominant modes form longitudinal acoustic waves along the fiber, approaching the extensional material velocity c_E (Fig. 6). This attenuation is usually called geometrical attenuation [41] because the strains in the SMF change with the fiber radius, achieving reduced amplitude in the fiber core. Note in Fig. 7 that both radial and axial strains are considerably reduced in this band. Losses caused by elastic friction, hysteresis and scattering due to the materials' grain size are negligible in the simulations for the considered frequency range and fiber length [17,55]. Nevertheless, these losses might become relevant for other kind of fibers with low silica purity or frequencies in which the material's grain size is equal to one third of an acoustic wavelength [55]. The predominant geometrical attenuation bands are therefore the main cause of the reduced optical phase, power, or sensitivity of fiber sensors, which depend on the acoustically induced strains in the fiber core [15,17];

(f) Resonances: in summary, all the propagating modes interact inside the fiber inducing a large strain field at the resonance frequencies. Closer modal wavenumbers increase the beat amplitude and period as resonance is approached [54]. The largest beatlength values are graphically observed as peaks in the FFT spectra in Fig. 5. These peaks are caused by close values of the modes' wavenumbers in Fig. 3, inducing the resonance peaks around 29 MHz and 68 MHz in Fig. 7 (the beatlengths indicate the modal interactions contributing to the generation of each resonance). The attenuation band is the transition range between the two resonances. In other words, resonances correspond to the frequencies in which the acoustic modes achieve a maximum constructive interference (peaks) and destructive interference (notches) in the fiber's cross section. The induced strains in the fiber core indicate that the optical phase-shift response of current optoacoustic sensors is mainly determined by beatlengths of axially symmetric modes (Fig. 7). Variations at the resonance peaks and bandwidths are caused by distinct boundary conditions, such as, asymmetric excitation and use of different interaction lengths, which might induce birefringence and excitation of co-propagating torsional modes. Overall, high agreement of the demonstrated FEM simulations with previous experimental devices shows that the asymmetric excitation has minimal influence to change the resonances and attenuation bands. This is because the resonances strongly depend on the fiber geometry and material, requiring structural waveguide modification to produce significant changes in the frequency response.

(g) Transverse acoustic resonances caused by optically induced non-linear effects, such as, Brillouin scattering, are generated by a completely different mechanism compared to the resonances in our study. Several narrow resonance lines are observed from the light scattering on the excited guided acoustic modes. The acoustic waves are usually generated in the core employing high optical powers and long fiber lengths. The resulting radial modes or mixed torsional-radial modes do not fully interfere inducing distinct narrowband resonant shapes in the spectrum [20,21]. The thermally excited modes do not contain axial components differing from the modes investigated in our study, which induce broadband resonances. We consider a short fiber length (1 cm) operating in a low optical power linear regime, in which the acoustic source is coupled on the fiber surface. These features are based on most of the acousto-optic and optoacoustic devices described in the Introduction. Overall, useful details about the characterization of resonances caused by optically induced non-linear effects are found in the Refs. [20,21].

3) Calculation of acoustic parameters required to modulate high frequency acousto-optic modulators and fiber sensors: this study provides the acoustic parameters for a wide range of fiber-based applications employing ultrasound up to 80 MHz, such as those presented in the Introduction and discussed in Section 2.2. The modal wavenumbers k, phase and group velocities, c_P and c_g are directly provided in Fig. 3(a) and 4(d). The modes' wavelengths λ_a and beatlengths B_a are given in the FFT spectra in Fig. 5 (these parameters can be graphically estimated from the pictures at any given frequency f). The spectral information is independent of the fiber length and excitation magnitude applied to the SMF, being useful to estimate the wavenumbers k and velocities c_P and c_g from an application-oriented frequency response. Acoustic impedances can be derived from the velocities as $Z_m = \rho c_g$, to predict transmission or reflection at layers surrounding the fiber surface [15,41]. The modulated reflectivity and wavelength of Bragg gratings are estimated with the acoustic period λ_a or beat B_a employing Eqs. (19)-(21). The optical phase-shift response is evaluated with Eqs. (17) and (18) employing the simulated radial and axial strains in the fiber core (Fig. 7). Overall, the acoustic parameters can be used in combination with other numerical methods, e.g., the transfer matrix method, to simulate the modulated reflection spectrum of FBGs [43,44].

4) Minimizing acoustic dispersion and resonances by changing the fiber geometry and material: broadband optoacoustic sensors demand constant or flat sensitivity response over a wide frequency range. It is achieved by changes in the SMF geometry and material. The use of fiber diameters smaller than the acoustic wavelength reduces the modes' number, preventing beatlengths and resonances. The SMF cross section is reduced by employing traditional cladding etching and fiber tapering techniques [8,49]. Alternatives include the use of polymer optical fibers [15] and microstructured optical fibers [1,2,27]. Recent studies show that suspended core fibers (SCFs) composed of a tiny core surrounded by large air holes are promising to reduce multimode propagation in the fiber core, increasing acousto-optic interaction at frequencies higher than 50 MHz. The geometry of SCFs can be adjusted to confine simultaneously acoustic and optical powers inside the fiber. The numerical methodology discussed in this study can be applied to evaluate SCFs and other fibers with complex geometries, in which the current analytical or semi-analytical methods developed to model solid cylinders are not possible.

5) Beatlength-induced acoustic gratings in optical fibers: long period gratings (LPGs) are characterized by a periodic modulation of the refractive index along the fiber, with periods usually in the range of 400 – 500 μm [51]. Two propagating optical modes interacting with the grating efficiently couple energy if their beatlength matches in phase with the period of the periodic modulation (Eq. (21)). Changes in the resonant condition is used to monitor applied deformation or temperature. Like the optical LPGs, the resonant notches around the resonances of 29 and 68 MHz in Fig. 6(a) are analogous to dynamically induced

acoustic LPGs along the fiber, with periods defined by the beatlengths. Changes in the resonances caused by external measurands are also expected. The acoustic LPG conversely transfers energy from the fiber cladding to the core. Previous studies show that even the dispersion of the fundamental acoustic mode at 10.9 MHz is efficient to produce relevant coupling and modulation of optical modes [23]. Improved acoustic filtering and flat spectral equalization of current fiber-based devices are achieved by the inscription of permanent LPGs. The modulation of the SMF refractive index is adjustable with high spatial resolution by employing CO_2, femtosecond lasers or electrical discharge techniques [52,56,57]. Modal coupling can therefore be tuned by the LPG to improve the sensor's sensitivity mainly in the high attenuation range from 40 to 60 MHz.

8. Conclusion

We have numerically characterized the resonances induced by the interference of high frequency axially symmetric acoustic modes inside an optical fiber for the first time. The multimode propagation is evaluated along 1 cm standard fiber employing the finite element method. 2D and 3D modeling techniques to evaluate complex ultrasonic fields up to 80 MHz are demonstrated. The simulated dispersion curves are validated with accuracies higher than 99.9 % compared to the Pochhammer-Chree analytical values.

Vibration patterns and dispersion parameters of three acoustic modes are independently computed employing the 2D modal analysis study and the 90° reduced-domain symmetric geometry. The modes are further excited along the 3D fiber device and the overlapped waveforms are assessed at the fiber surface, cladding, and core. Modal dispersion and induced beatlengths are simultaneously evaluated with the peak-to-peak method (APP) and the 2D fast Fourier transform (FFT). The acoustically induced displacements and strains are spatially characterized inside the fiber. The results reveal resonances caused by the modes interfering at specific beatlengths, indicating that axially symmetric waves have a strong influence in the operation of current optoacoustic sensors. Modes with similar group velocities transfer energy between the fiber surface and core, particularly in the regions of 29 and 68 MHz. In the high attenuation range of 40 – 60 MHz, the modes weakly interact in the fiber core. The frequency-tunable modal redistribution in the fiber is promising for spatial division multiplexers and couplers. The suitable equalization of the sensor's sensitivity over a broadband frequency range might be achieved by the inscription of permanent LPGs in the SMF, coupling energy to the fiber core over the attenuation bands. Alternatively, fibers with different materials and geometries are promising to improve the acousto-optic interaction and the noise-limited pressure resolution.

In summary, FEM and FFT methods provide a practical and intuitive tool to characterize the changing complex ultrasonic wave patterns in optical fibers with increasing frequency, allowing the spatial and spectral characterization of multimode interference along the fiber. Significant acoustic parameters required for a wide range of applications employing standard fibers may be obtained. The numerical methods can be applied to evaluate fibers with complex geometries, in which the analytical and semi-analytical approaches based on ideal solid cylinders are not possible.

CRediT authorship contribution statement

Ricardo E. da Silva: Investigation, Methodology, Formal analysis, Validation, Writing – original draft, Writing – review & editing. **David J. Webb:** Investigation, Writing – review & editing, Funding acquisition, Resources.

Declaration of Competing Interest

The authors declare that they have no known competing financial interests or personal relationships that could have appeared to influence the work reported in this paper.

Data availability

Data will be made available on request.

Acknowledgements

This work was funded by the European Union's Horizon 2020 research and innovation programme under the Marie Sklodowska-Curie grant agreement No 713694. We acknowledge the use of Athena at HPC Midlands+, which was funded by the EPSRC on grant EP/P020232/1 as part of the HPC Midlands Plus consortium.

References

[1] R.E. Silva, D.J. Webb, Ultra-efficient in-core acoustic waves in suspended core fiber for high frequency fiber-optic ultrasonic devices, Appl. Phys. Express. 14 (2021), 087003. https://doi.org/10.35848/1882-0786/AC17D5.
[2] R.E. Silva, E. Manuylovich, N. Sahoo, M. Becker, M. Rothhardt, H. Bartelt, D. J. Webb, Highly efficient side-coupled acousto-optic modulation of a suspended core fiber Bragg grating, IEEE Photonics Technol. Lett. 33 (2021) 1379–1382, https://doi.org/10.1109/LPT.2021.3123258.
[3] J. Lu, F. Shi, J. Xu, L. Meng, L. Zhang, P. Cheng, X. Zhou, F. Pang, X. Zeng, Recent progress of dynamic mode manipulation via acousto-optic interactions in few-mode fiber lasers: Mechanism, device and applications, Nanophotonics. 10 (2021) 983–1010, https://doi.org/10.1515/nanoph-2020-0461.
[4] I.B. Javorsky, R.E. Silva, A.A.P. Pohl, Wavelength tunable filter based on acousto-optic modulation of a double-core fiber, IEEE Photonics Technol. Lett. 31 (2019) 1135–1138, https://doi.org/10.1109/LPT.2019.2919483.
[5] A.A.P. Pohl, R.A. Oliveira, R.E. da Silva, C.A.F. Marques, P.T. Neves, K. Cook, J. Canning, R.N. Nogueira, Advances and new applications using the acousto-optic effect in optical fibers, Photonic Sens. 3 (1) (2013) 1–25, https://doi.org/10.1007/s13320-013-0100-0.
[6] R.E. Silva, T. Tiess, M. Becker, T. Eschrich, M. Rothhardt, M. Jäger, A.A.P. Pohl, H. Bartelt, Acousto-optic modulation of a fiber Bragg grating in suspended core fiber for mode-locked all-fiber lasers, Laser Phys. Lett. 12 (4) (2015) 045101, https://doi.org/10.1088/1612-2011/12/4/045101.
[7] I.L. Villegas, C. Cuadrado-Laborde, J. Abreu-Afonso, A. Díez, J.L. Cruz, M. A. Martínez-Gámez, M.V. Andrés, Mode-locked Yb-doped all-fiber laser based on in-fiber acoustooptic modulation, Laser Phys. Lett. 8 (2011) 227–231, https://doi.org/10.1002/lapl.201010116.
[8] M. Delgado-Pinar, D. Zalvidea, A. Diez, P. Perez-Millan, M. Andres, Q-switching of an all-fiber laser by acousto-optic modulation of a fiber Bragg grating, Opt. Express. 14 (2006) 1106–1112, https://doi.org/10.1364/OE.14.001106.
[9] N.E. Fisher, D.J. Webb, C.N. Pannell, D.A. Jackson, L.R. Gavrilov, J.W. Hand, L. Zhang, I. Bennion, Ultrasonic hydrophone based on short in-fiber Bragg gratings, Appl. Opt. 37 (1998) 8120, https://doi.org/10.1364/ao.37.008120.
[10] G.M. Ma, H.Y. Zhou, C. Shi, Y.B. Li, Q. Zhang, C.R. Li, Q. Zheng, Distributed partial discharge detection in a power transformer based on phase-shifted FBG, IEEE Sens. J. 18 (2018) 2788–2795, https://doi.org/10.1109/JSEN.2018.2803056.
[11] A. Cusano, P. Capoluongo, S. Campopiano, A. Cutolo, M. Giordano, F. Felli, A. Paolozzi, M. Caponero, Experimental modal analysis of an aircraft model wing by embedded fiber bragg grating sensors, IEEE Sens. J. 6 (2006) 67–77, https://doi.org/10.1109/JSEN.2005.854152.
[12] W. Ecke, I. Latka, R. Willsch, A. Reutlinger, R. Graue, Fibre optic sensor network for spacecraft health monitoring, Meas. Sci. Technol. 12 (2001) 974, https://doi.org/10.1088/0957-0233/12/7/339.
[13] P. Moyo, J.M.W. Brownjohn, R. Suresh, S.C. Tjin, Development of fiber Bragg grating sensors for monitoring civil infrastructure, Eng. Struct. 27 (2005) 1828–1834, https://doi.org/10.1016/J.ENGSTRUCT.2005.04.023.
[14] L. Dziuda, F.W. Skibniewski, M. Krej, J. Lewandowski, Monitoring respiration and cardiac activity using fiber Bragg grating-based sensor, IEEE Trans. Biomed. Eng. 59 (2012) 1934–1942, https://doi.org/10.1109/TBME.2012.2194145.
[15] T. Berer, I.A. Veres, H. Grün, J. Bauer-Marschallinger, K. Felbermayer, P. Burgholzer, Characterization of broadband fiber optic line detectors for photoacoustic tomography, J. Biophotonics. 5 (2012) 518–528, https://doi.org/10.1002/JBIO.201100110.
[16] R. Shnaiderman, G. Wissmeyer, M. Seeger, D. Soliman, H. Estrada, D. Razansky, A. Rosenthal, V. Ntziachristos, Fiber interferometer for hybrid optical and optoacoustic intravital microscopy, Optica 4 (10) (2017) 1180, https://doi.org/10.1364/OPTICA.4.001180.
[17] I.A. Veres, P. Burgholzer, T. Berer, A. Rosenthal, G. Wissmeyer, V. Ntziachristos, Characterization of the spatio-temporal response of optical fiber sensors to incident spherical waves, J. Acoust. Soc. Am. 135 (4) (2014) 1853–1862, https://doi.org/10.1121/1.4868391.
[18] G. Wissmeyer, D. Soliman, R. Shnaiderman, A. Rosenthal, V. Ntziachristos, All-optical optoacoustic microscope based on wideband pulse interferometry, Opt. Lett. 41 (9) (2016) 1953, https://doi.org/10.1364/OL.41.001953.

[19] R.E. Silva, M.A.R. Franco, P.T. Neves, H. Bartelt, A.A.P. Pohl, Detailed analysis of the longitudinal acousto-optical resonances in a fiber Bragg modulator, Opt. Express. 21 (2013) 6997–7007, https://doi.org/10.1364/OE.21.006997.
[20] L.A. Sánchez, A. Díez, J.L. Cruz, M.V. Andrés, High accuracy measurement of Poisson's ratio of optical fibers and its temperature dependence using forward-stimulated Brillouin scattering, Opt. Express 30 (1) (2022) 42–52, https://doi.org/10.1364/OE.442295.
[21] R.M. Shelby, M.D. Levenson, P.W. Bayer, Guided acoustic-wave Brillouin scattering, Phys. Rev. B. 31 (8) (1985) 5244–5252, https://doi.org/10.1103/PhysRevB.31.5244.
[22] H.E. Engan, B.Y. Kim, J.N. Blake, H.J. Shaw, Propagation and optical interaction of guided acoustic waves in two-mode optical fibers, J. Light. Technol. 6 (1988) 428–436, https://doi.org/10.1109/50.4020.
[23] R.E. Silva, T. Tiess, M. Becker, T. Eschrich, M. Rothhardt, M. Jäger, A.A.P. Pohl, H. Bartelt, All-fiber 10 MHz acousto-optic modulator of a fiber Bragg grating at 1060 nm wavelength, Opt. Express. 23 (2015) 25972–25978, https://doi.org/10.1364/OE.23.025972.
[24] I.A. Veres, G. Flockhart, G. Pierce, B. Culshaw, T. Berer, H. Grün, P. Burgholzer, B. Reitinger, Numerical and analytical modeling of optical fibers for ultrasound detection, IEEE Int. Ultrason. Symp. IUS. (2011) 520–523, https://doi.org/10.1109/ULTSYM.2011.0125.
[25] A.D. Puckett, M.L. Peterson, A semi-analytical model for predicting multiple propagating axially symmetric modes in cylindrical waveguides, Ultrasonics. 43 (2005) 197–207, https://doi.org/10.1016/j.ultras.2004.04.008.
[26] A. Puckett, An experimental and theoretical investigation for axially symmetric wave propagation in thick cylindrical waveguides, 2004. http://digitalcommons.library.umaine.edu/etd/285 (accessed June 13, 2021).
[27] K. Saitoh, M. Koshiba, Full-vectorial imaginary-distance beam propagation method based on a finite element scheme: application to photonic crystal fibers, IEEE J. Quantum Electron. 38 (2002) 927–933, https://doi.org/10.1109/JQE.2002.1017609.
[28] R.A. Oliveira, P.T. Neves Jr., J.T. Pereira, J. Canning, A.A.P. Pohl, Vibration mode analysis of a silica horn–fiber Bragg grating device, Opt. Commun. 283 (2010) 1296–1302, https://doi.org/10.1016/j.optcom.2009.11.035.
[29] C. Yang, L. Ye, Z. Su, M. Bannister, Some aspects of numerical simulation for Lamb wave propagation in composite laminates, Compos. Struct. 75 (2006) 267–275, https://doi.org/10.1016/J.COMPSTRUCT.2006.04.034.
[30] R.E. Silva, M.A.R. Franco, H. Bartelt, A.A.P. Pohl, Numerical characterization of piezoelectric resonant transducer modes for acoustic wave excitation in optical fibers, Meas. Sci. Technol. 24 (9) (2013) 094020, https://doi.org/10.1088/0957-0233/24/9/094020.
[31] R.E. Silva, A. Hartung, M. Rothhardt, A.A.P. Pohl, H. Bartelt, Detailed numerical investigation of the interaction of longitudinal acoustic waves with fiber Bragg gratings in suspended-core fibers, Opt. Commun. 344 (2015) 43–50, https://doi.org/10.1016/j.optcom.2015.01.037.
[32] A.C. Hladky-Hennion, Finite element analysis of the propagation of acoustic waves in waveguides, J. Sound Vib. 194 (1996) 119–136, https://doi.org/10.1006/JSVI.1996.0349.
[33] P. Hora, O. Červená, Determination of Lamb wave dispersion curves by means of Fourier transform, Appl. Comput. Mech. 6 (2012) 5–16. https://www.kme.zcu.cz/acm/acm/article/view/149.
[34] R.E. Silva, M.A. Franco, H. Bartelt, A.A.P. Pohl, Numerical characterization of an acousto-optic ring sensor for measuring D-Glucose concentrations. Work. Spec. Opt. Fibers Their Appl., OSA, Washington, D.C., 2013 p. F2.20. https://doi.org/10.1364/WSOF.2013.F2.2.
[35] L. Pochhammer, "On the velocity of propagation of small vibrations in an isotropic cylinder of infinite length". Ueber die fortpflanzungsgeschwindigkeiten kleiner schwingungen in einem unbegrenzten isotropen kreiscylinder, J. Fur Die Reine Und Angew. Math. 1876 (1876) 324–336, https://doi.org/10.1515/crll.1876.81.324.
[36] C. Chree, Longitudinal vibrations of a circular bar, Q. J. Pure Appl. Math. 21 (1886) 287–289.
[37] R.M. Davies, A critical study of the Hopkinson pressure bar, Philos. Trans. R. Soc. London. Ser. A, Math. Phys. Sci. 240 (1948) 375–457, https://doi.org/10.1098/rsta.1948.0001.
[38] J. Zemanek, An experimental and theoretical investigation of elastic wave propagation in a cylinder, J. Acoust. Soc. Am. 51 (1B) (1972) 265–283, https://doi.org/10.1121/1.1912838.
[39] M.L. Peterson, Prediction of longitudinal disturbances in a multimode cylindrical waveguide, Exp. Mech. 39 (1999) 36–42, https://doi.org/10.1007/BF02329299.
[40] A.D. Puckett, M.L. Peterson, Individual longitudinal Pochhammer-Chree modes in observed experimental signals, Acoust. Res. Lett Online 6 (2005) 268–273, https://doi.org/10.1121/1.2033088.
[41] J. Achenbach, Wave Propagation in Elastic Solids, 1st ed.,, Elsevier Science, 1984.
[42] R.N. Thurston, Elastic waves in rods and clad rods, J. Acoust. Soc. Am. 64 (1978) 1–37, https://doi.org/10.1121/1.381962.
[43] M. Redwood, Mechanical Waveguides: the Propagation of Acoustic and Ultrasonic Waves in Fluids and Solids With Boundaries, Pergamon Press, New York, 1960. https://catalog.princeton.edu/catalog/9915017573506421.
[44] M. Redwood, Velocity and attenuation of a narrow-band, high-frequency compressional pulse in a solid wave guide, J. Acoust. Soc. Am. 31 (4) (1959) 442–448, https://doi.org/10.1121/1.1907732.
[45] B. Masserey, C. Raemy, P. Fromme, High-frequency guided ultrasonic waves for hidden defect detection in multi-layered aircraft structures, Ultrasonics. 54 (2014) 1720–1728, https://doi.org/10.1016/j.ultras.2014.04.023.
[46] B.W. Ti, W.D. O'Brien, J.G. Harris, Measurements of coupled Rayleigh wave propagation in an elastic plate, J. Acoust. Soc. Am. 102 (3) (1997) 1528–1531, https://doi.org/10.1121/1.419554.
[47] B. Masserey, P. Fromme, On the reflection of coupled Rayleigh-like waves at surface defects in plates, J. Acoust. Soc. Am. 123 (2008) 88–98, https://doi.org/10.1121/1.2805668.
[48] J. Dorighi, S. Krishnaswamy, J.D. Achenbach, Response of an embedded fiber optic ultrasound sensor, J. Acoust. Soc. Am. 101 (1) (1997) 257–263, https://doi.org/10.1121/1.417997.
[49] W.F. Liu, P.S.J. Russell, L. Dong, 100% efficient narrow-band acoustooptic tunable reflector using fiber Bragg grating, J. Light. Technol. 16 (1998) 2006–2009, https://doi.org/10.1109/50.730362.
[50] COMSOL Multiphysics Reference Manual 5.4, (2018). https://doc.comsol.com/5.4/doc/com.comsol.help.comsol/COMSOL_ReferenceManual.pdf.
[51] J.S. Petrovic, H. Dobb, V.K. Mezentsev, K. Kalli, D.J. Webb, I. Bennion, Sensitivity of LPGs in PCFs fabricated by an electric arc to temperature, strain, and external refractive index, J. Light. Technol. 25 (2007) 1306–1312, https://doi.org/10.1109/JLT.2007.893912.
[52] MATLAB, Curve Fitting Toolbox Documentation, (n.d.). https://www.mathworks.com/help/curvefit/ (accessed January 17, 2022).
[53] J.A. Parker, R.V. Kenyon, D.E. Troxel, Comparison of interpolating methods for image resampling, IEEE Trans. Med. Imaging. 2 (1983) 31–39, https://doi.org/10.1109/TMI.1983.4307610.
[54] B. Bharat, V.R. Sonti, Resonance and beating phenomenon in a nonlinear rigid cylindrical acoustic waveguide: the axisymmetric mode, J. Sound Vib. 458 (2019) 262–275, https://doi.org/10.1016/j.jsv.2019.06.025.
[55] W.P. Mason, H.J. McSkimin, Attenuation and scattering of high frequency sound waves in metals and glasses, J. Acoust. Soc. Am. 19 (1947) 464–473, https://doi.org/10.1121/1.1916504.
[56] A. Diez, G. Kakarantzas, T.A. Birks, P.S.J. Russell, Acoustic stop-bands in periodically microtapered optical fibers, Appl. Phys. Lett. 76 (23) (2000) 3481–3483, https://doi.org/10.1063/1.126684.
[57] D. Hu, H. Xuan, Z. Yu, D.Y. Wang, B. Liu, J. He, A. Wang, Acoustic fiber bragg grating and its application in high temperature sensing, IEEE Sens. J. 18 (2018) 9576–9583, https://doi.org/10.1109/JSEN.2018.2867604.